J. Fluid Mech. (1978), *vol.* 89, *part* 3, *pp.* 535–552
Printed in Great Britain

Triple-deck solutions for viscous supersonic and hypersonic flow past corners

By D. P. RIZZETTA,† O. R. BURGGRAF AND RICHARD JENSON‡

Department of Aeronautical and Astronautical Engineering, The Ohio State University, Columbus, Ohio 43210

(Received 29 December 1977)

A viscous–inviscid interaction is produced when a compressible laminar boundary layer encounters a corner. The correct mathematical structure for such interactions at large Reynolds number is given by the asymptotic triple-deck theory. In the present work the triple-deck equations for supersonic and hypersonic flows are solved for both compression and expansion corners. Results are presented for a range of corner angles, including separated cases, and are compared with experimental data and with finite Reynolds number calculations based on an interacting boundary-layer model.

1. Introduction

When a supersonic stream flowing over a plane surface encounters a compressive disturbance of sufficient magnitude, the flow will separate from the wall. The point at which the boundary layer separates has been commonly observed to occur well upstream of the disturbance, generating compression waves in the mainstream. Downstream of separation the boundary layer develops as a free shear layer beneath which lies a region of slowly circulating fluid. If the compressive disturbance has been caused by a compression ramp, the free shear layer will reattach to the wall downstream of the corner, generating additional compression waves in the external flow. This description applies to the situation in which the mainstream is uniform and the wall downstream of the corner is sufficiently long, and has been studied in detail experimentally by Chapman, Kuehn & Larsen (1958) and others. The observation that the separation point lies well upstream of the corner contradicts the inherent nature of Prandtl's boundary-layer theory. However Crocco & Lees (1952) have shown that coupling the pressure gradient of the external inviscid flow to the displacement thickness of the boundary layer permits upstream influence to be consistent with the boundary-layer equations. This concept led to the approximate integral methods of Lees & Reeves (1964) and others. On the basis of the original ideas of Lighthill (1950, 1953), a rational self-consistent mathematical structure (dubbed the triple deck) has been developed for viscous–inviscid interacting flows by Stewartson & Williams (1969). In independent papers an identical structure was arrived at also by Neiland (1969) and by Messiter (1970), and recently has been extended to include the case of a hypersonic mainstream by Brown, Stewartson & Williams (1975). Since its original

† Present address: The Boeing Company, Seattle, Washington.

‡ Present address: Department of Aerospace Engineering, Texas A & M University, College Station, Texas 77840.

formulation, this analysis has been applied to numerous viscous–inviscid interaction problems, many of which have been summarized by Stewartson (1974).

The basic problem to be considered here is that of a viscous compressible fluid flowing supersonically past a flat-plate/ramp combination at high Reynolds number Re. If the ramp angle α^* is of order $Re^{-\frac{1}{4}}$, a triple-deck structure develops within a longitudinal distance of order $Re^{-\frac{3}{8}}$ centred about the plate/ramp juncture. Upstream of this region it is assumed that the flow is laminar and fully developed. Within the longitudinal interaction distance there are three distinct vertically scaled regions in which different physical processes dominate. Correspondingly, three separate scalings of the dependent and independent variables in each of the regions are necessary, resulting in the asymptotic equations which govern the physical processes involved in each of these three layers (or decks). The distinct solutions in the three decks are related by matching conditions, obtained by the method of matched asymptotic expansions. The mathematical formulation is outlined in § 2, the numerical procedures are described in § 3, and the results for compression and expansion ramps are discussed in § 4.

2. The triple-deck structure

Stewartson's triple-deck structure is depicted schematically in figure 1. The main deck has a transverse scale $O(Re^{-\frac{1}{2}})$ and consists of fluid in the upstream boundary layer passing through the corner region in which the interaction takes place. Because the interaction region is short, the dominant mechanism in the main deck is an inviscid turning of the upstream boundary layer. Thus the leading-order equations governing the flow in the main deck are simply those of vertical displacement of the streamlines. The upper deck has a length scale $O(Re^{-\frac{3}{8}})$ in both the transverse and the longitudinal direction, and consists of fluid which is disturbed by flow in the interaction region through outward propagation of Mach waves. Here the dominant process is irrotational as well as inviscid, so that to leading order the governing equations are the Prandtl–Glauert equations. The lower deck is characterized by viscous flow and has a vertical scale $O(Re^{-\frac{5}{8}})$. Because this layer is extremely thin, the flow here is incompressible and, after appropriate rescaling of the variables, the leading-order equations are the usual incompressible boundary-layer equations, but with modified boundary conditions. The wall boundary conditions are the customary 'no-slip' conditions, but the condition at the outer edge comes from matching to the rotational inviscid main deck, rather than to an irrotational inviscid outer flow. In turn, the main deck is matched to the upper deck and thus assumes the passive role of transmitting streamline displacement from the lower deck to the upper deck and pressure perturbations from the upper deck to the lower deck. Hence the upper deck provides a relationship between the pressure and streamline displacement at the outer edge of the lower deck.

As the asymptotic equations governing the flow in the main and upper decks permit simple analytical solutions, the problem is reduced to solving the incompressible boundary-layer equations (with appropriate boundary conditions) in the lower deck. To first order the pressure and flow angle in the main deck are independent of distance from the wall. Consequently, matching the solutions in the three decks implies that the pressure/flow-angle relation at the base of the upper deck can be applied directly

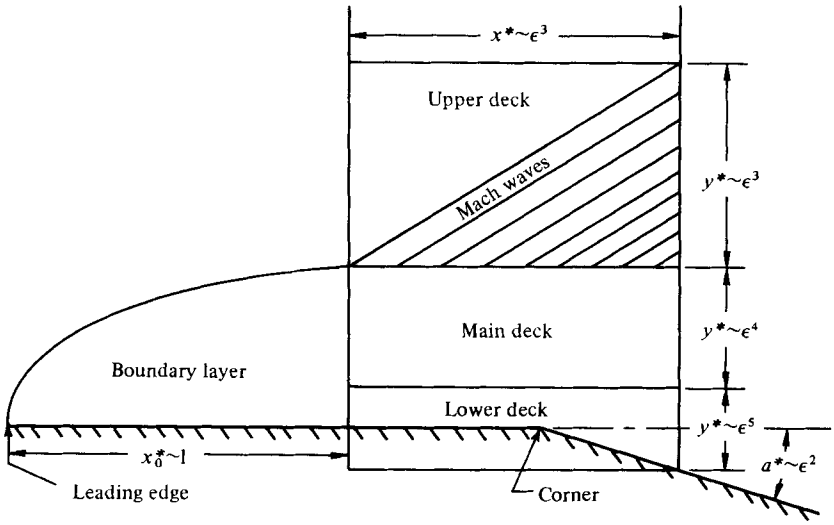

FIGURE 1. Triple-deck structure for corner-flow problem (note: $\epsilon = Re^{-\frac{1}{8}}$).

as a boundary condition at the top of the lower deck. For details of the argument, see Stewartson & Williams (1969). The normal pressure gradient in the main deck appears in higher-order terms, as demonstrated by Brown & Williams (1975).

Physical quantities are denoted by an asterisk, free-stream values by the subscript ∞ and wall values by the subscript w. The co-ordinate parallel to the plate is x^* with origin at the leading edge and that transverse to the plate is y^*. The distance from the leading edge to the corner is denoted x_0^*. The streamwise and transverse velocity components are u^* and v^*, and p^* is the pressure. Define the Reynolds number Re as $\rho_\infty^* u_\infty^* x_0^*/\mu_\infty^*$ and let $\epsilon = Re^{-\frac{1}{8}}$. Then, following Stewartson & Williams (1969), non-dimensional lower-deck variables are introduced as

$$X = (x^* - x_0^*)/\epsilon^3 a, \quad a = x_0^* C^{\frac{3}{8}} \lambda^{-\frac{5}{4}} (M_\infty^2 - 1)^{-\frac{3}{8}} (T_w^*/T_\infty^*)^{\frac{3}{2}}, \tag{2.1a}$$

$$Y = y^*/\epsilon^5 b, \quad b = x_0^* C^{\frac{5}{8}} \lambda^{-\frac{3}{4}} (M_\infty^2 - 1)^{-\frac{1}{8}} (T_w^*/T_\infty^*)^{\frac{3}{2}}, \tag{2.1b}$$

$$t = dt^*/\epsilon^2 ab, \quad d = x_0^* u_\infty^* C^{\frac{3}{4}} \lambda^{-\frac{1}{2}} (M_\infty^2 - 1)^{-\frac{1}{4}} (T_w^*/T_\infty^*)^2, \tag{2.1c}$$

$$\alpha = a\alpha^*/\epsilon^2 b, \quad U = bu^*/\epsilon d, \quad V = av^*/\epsilon^3 d, \tag{2.1d–f}$$

$$P = (p^* - p_\infty^*)/\epsilon^2 c, \quad c = \rho_\infty^* u_\infty^{*2} C^{\frac{1}{4}} \lambda^{\frac{1}{2}} (M_\infty^2 - 1)^{-\frac{1}{4}}. \tag{2.1g}$$

Here α^* is the ramp angle, C the Chapman–Rubesin constant ($C = \mu_w^* T_\infty^*/\mu_\infty^* T_w^*$), t^* physical time and λ has the value 0·33206 associated with the wall shear of the Blasius solution. The equations of motion for the lower deck then reduce to the classical boundary-layer form:

$$\partial U/\partial X + \partial V/\partial Y = 0, \tag{2.2a}$$

$$\frac{\partial U}{\partial t} + U\frac{\partial U}{\partial X} + V\frac{\partial U}{\partial Y} = -\frac{\partial P}{\partial X} + \frac{\partial^2 U}{\partial Y^2}, \tag{2.2b}$$

where P is independent of Y. Anticipating a time-dependent numerical scheme to obtain steady-state solutions for ramp flows, the unsteady lower-deck equations have been used.

The boundary conditions necessary for a complete statement of the problem are as follows. At the wall the traditional conditions apply:

$$U = V = 0 \quad \text{on} \quad \begin{cases} Y = 0, & X \leqslant 0, \\ Y = \alpha X, & X \geqslant 0. \end{cases} \tag{2.3a}$$

The upstream boundary condition is obtained by matching to the undisturbed profile, i.e. the compressible Blasius solution. Rewriting the Blasius solution in the non-dimensional lower-deck variables and taking the limit $\epsilon \to 0$ for Y fixed yields the first-order matching condition:

$$U \to Y \quad \text{as} \quad X \to -\infty. \tag{2.3b}$$

For $Y \to \infty$, the lower-deck solution must match conditions at the base of the main deck. This requires

$$\lim_{Y \to \infty} (U - Y) = -\int_{-\infty}^{X} P\,d\xi. \tag{2.3c}$$

See Stewartson & Williams (1969) for details on the derivation of (2.3*c*).

Downstream of interaction, we require that the flow should return to an undisturbed state. This necessitates imposition of a downstream boundary condition to ensure uniqueness and prevent the appearance of spurious eigenfunctions. Once again matching to the Blasius solution, we obtain

$$U \to Y - \alpha X \quad \text{as} \quad X \to +\infty, \tag{2.3d}$$

which completes the statement of the problem.

It should be noted that it has been assumed that the magnitude of the corner angle $|\alpha^*|$ is of order $Re^{-\frac{1}{4}}$. For compression-ramp angles of this order, as long as reattachment occurs within the $Re^{-\frac{3}{8}}$ length scaling, the downstream conditions are known and non-uniqueness problems due to reversed flow as $X \to +\infty$ do not arise. For smaller angles, separation does not occur. On the other hand, if the angle is larger than $O(Re^{-\frac{1}{4}})$ there evolves a more complex structure which has been analysed by Burggraf (1975).

Since its original formulation, triple-deck theory has been modified to describe hypersonic interacting flows by Brown *et al.* (1975). The analysis accounts for a hypersonic main deck and obtains the pressure–displacement relationship through the tangent-wedge approximation. While the non-dimensionalization of the dependent and independent variables (2.1) is now altered, the lower-deck equations and boundary conditions remain intact with the exception of (2.3*c*). This becomes

$$\lim_{Y \to \infty} (U - Y) = -\int_{-\infty}^{X} P\,d\xi - \sigma P. \tag{2.4}$$

The parameter σ is proportional to the conventional hypersonic interaction parameter χ evaluated at the location of the upstream origin of interaction x_s^*:

$$\sigma = \{4\gamma^3\lambda^5\Delta^4\chi/[\beta(\gamma-1)^2 p_0^{\frac{1}{2}} S_w^6]\}^{\frac{1}{4}}, \tag{2.5a}$$

where

$$\Delta = 2{\cdot}385 + 1{\cdot}721\,(S_w - 1), \quad \chi = M_\infty^3 C^{\frac{1}{2}}/(\rho_\infty u_\infty x_s^*/\mu_\infty)^{\frac{1}{2}}, \tag{2.5b, c}$$

$$\beta = [3\gamma - 1 + (\gamma+1)p_0]/\{(2\gamma)^{\frac{1}{2}}[(\gamma-1) + (\gamma+1)p_0]^{\frac{3}{2}}\}, \tag{2.5d}$$

$$S_w = [2/(\gamma-1)M_\infty^2](T_w/T_\infty), \quad p_0 = p^*(x_s^*)/p_\infty. \tag{2.5e, f}$$

Thus, for the lower-deck equations, $\sigma \to 0$ corresponds to the supersonic case. The reader is referred to Brown *et al.* (1975) for a more detailed discussion of these results, including the modified definitions of the dependent and independent variables.

3. The numerical procedure

Steady-flow solutions of (2.2*a*, *b*) were obtained as the large-time limit of the unsteady flow produced when the ramp angle is impulsively increased from zero to α at time $t = 0$. The numerical scheme, to be briefly summarized here, is presented in more detail by Rizzetta (1976). Application of the wall boundary conditions is simplified if the geometry is transformed according to Prandtl's transposition theorem. For this purpose, the following variables are defined:

$$Z = Y - \alpha X H(X), \quad W = V - \alpha U H(X), \tag{3.1), (3.2}$$

where $H(X)$ is the Heaviside step function. Under this transformation, the continuity and momentum equations are invariant (see Rosenhead 1963).

The problem is now formulated in terms of the non-dimensional shear stress $\tau = \partial U/\partial Y = \partial U/\partial Z$ such that the pressure is explicitly eliminated from the equations. Differentiating the momentum equation with respect to Z and applying continuity results in

$$\frac{\partial \tau}{\partial t} + U\frac{\partial \tau}{\partial X} + W\frac{\partial \tau}{\partial Z} = \frac{\partial^2 \tau}{\partial Z^2}. \tag{3.3}$$

In terms of τ, the boundary conditions at infinity simplify to

$$\tau \to 1 \quad \text{as} \quad X \to \pm\infty, \quad 0 \leqslant Z < \infty \tag{3.4a}$$

and

$$\tau \to 1 \quad \text{as} \quad Z \to \infty, \quad -\infty < X < \infty. \tag{3.4b}$$

The pressure–displacement interaction condition is derived by differentiating (2.4) twice with respect to X and eliminating the pressure by use of the wall compatibility condition (i.e. $dP/dX = [\partial\tau/\partial Z]_{z=0}$). This yields

$$\left.\frac{\partial \tau}{\partial Z}\right|_{z=0} + \sigma \left.\frac{\partial^2 \tau}{\partial X\,\partial Z}\right|_{z=0} = -\frac{\partial^2}{\partial X^2}\int_0^\infty \tau\, dZ + \alpha\delta(X), \tag{3.5}$$

where $\delta(X)$ is the Dirac delta function. The elliptic nature of the problem is evident from the appearance of the operator $\partial^2/\partial X^2$ in the interaction condition, even though the lower-deck equations are parabolic and the upper-deck equations are hyperbolic.

It should be noted that the transposition of variables in (3.1) and (3.2) produces a discontinuity in W at $X = 0$, as well as the delta function in (3.5). Numerically, these are treated by introducing a double array for W at $X = 0\pm$ and by integrating (3.5) over X from $X = -\frac{1}{2}\Delta X$ to $X = +\frac{1}{2}\Delta X$.

The numerical method used to solve the unsteady shear transport equation, which is given by Jenson, Burggraf & Rizzetta (1975), employs the equation

$$\frac{\partial \tau}{\partial t} + \Delta t\left[\hat{U}\frac{\partial}{\partial X}\left(\frac{\partial \tau}{\partial t}\right) + \hat{W}\frac{\partial}{\partial Z}\left(\frac{\partial \tau}{\partial t}\right) - \frac{\partial^2}{\partial Z^2}\left(\frac{\partial \tau}{\partial t}\right)\right] = -\left[\hat{U}\frac{\partial \hat{\tau}}{\partial X} + \hat{W}\frac{\partial \hat{\tau}}{\partial Z} - \frac{\partial^2 \hat{\tau}}{\partial Z^2}\right]. \tag{3.6}$$

Here the circumflex denotes conditions at the previous time step. This scheme is semi-implicit in time, in that $\hat{U}$ and $\hat{W}$ are evaluated at the previous time step, while the spatial derivatives of τ are evaluated from backward differences in time.

More accurate central time differences would have been as easy to implement but the choice of backward differences was motivated by stability considerations. Since the unsteady solution was viewed solely as a computational device for obtaining the steady solution, the larger Δt-truncation error of this scheme is of no consequence. A time-explicit scheme was also tried, but was found to require much smaller time steps than the present scheme.

The computation is initiated at time $t = 0$ with the uniform shear flow $U = Z$. Equation (3.6) is then used to march in time to the steady-state solution. All Z derivatives are replaced by centred differences, but X derivatives are replaced by upwind differences in order to maintain stability in reversed-flow regions. Consequently, the scheme is second-order accurate in Z, but only first-order accurate in X. This accuracy may be improved by Richardson extrapolation to zero mesh width, as will be discussed in more detail later. At interior points of the numerical mesh τ is computed from (3.6). This requires solution of a tridiagonal matrix equation for $\partial\tau/\partial t$ at time t at each X station. Wall values of τ are then computed from (3.5). The U velocity component is obtained by integrating τ by the trapezoidal rule. W then follows from continuity employing centred differences except at $X = 0$, where forward and backward differences are used to allow for the discontinuity previously mentioned. Once the steady state has been achieved, P is computed by integration of the wall compatibility condition using the trapezoidal rule and noting that $P \to 0$ as $X \to -\infty$.

To avoid the use of an excessively long computational mesh, the upstream and downstream conditions (3.4a) were replaced by asymptotic expressions which describe the decay of τ to unity as $X \to \pm\infty$. Upstream, Stewartson & Williams (1969) have shown that

$$\tau \sim 1 - a_1 e^{\kappa X} f''(Z), \tag{3.7}$$

where κ is a known constant and f is a prescribed function. Numerically, this condition is applied in the form

$$\partial\tau/\partial X = \kappa(\tau - 1) \tag{3.8}$$

using a centred difference between the first two upstream X stations. Downstream, the proper asymptotic form for τ is given by Smith & Stewartson (1973) as

$$\tau \sim 1 + X^{-\frac{1}{3}} g''(\eta), \quad \eta = Z/X^{\frac{1}{3}}. \tag{3.9}$$

This condition is applied in the approximate form

$$\frac{\partial\tau}{\partial X} = \frac{2}{3}\left(\frac{1-\tau}{X}\right), \tag{3.10}$$

which becomes exact as $X \to \infty$ with Z fixed. A centred difference was used to apply (3.10) between the last two downstream X stations. The use of asymptotic boundary conditions allowed great reduction in the extent of the computational mesh, particularly downstream, where the algebraic decay is quite slow.

It should be noted that the wall condition (3.5) is regarded as a central feature of the numerical procedure. In finite-difference form this is expressed as

$$\left(\frac{\Delta X}{\Delta Z}\right)(\tau_{k,2} - \tau_{k,1}) + \left(\frac{\sigma}{2\Delta Z}\right)(\tau_{k+1,2} + \tau_{k-1,1} - \tau_{k+1,1} - \tau_{k-1,2})$$
$$= -\left(\frac{\Delta Z}{\Delta X}\right)\left[(\tfrac{1}{2}(\tau_{k+1,1} - 2\tau_{k,1} + \tau_{k-1,1}) + \sum_{j=2}^{m-1}(\tau_{k+1,j} - 2\tau_{k,j} + \tau_{k-1,j})\right] + \alpha\delta_k^{kc}. \tag{3.11}$$

Here $\tau_{k,j}$ refers to the value of τ at the kth X station and the jth Z station, $j = 1$ corresponds to $Z = 0$ and $j = m$ to the outer boundary, $k = kc$ refers to the corner location, and δ_k^{kc} is the Kronecker delta symbol. For the steady state, in which case $[\partial^2\tau/\partial Z^2]_{Z=0} = 0$, the truncation error is $O[(\Delta X)^2, (\Delta Z)^2]$ except at the corner. A detailed analysis along the lines of Goldstein (1930) indicates that the error at the corner is of order $(\Delta X)^{\frac{1}{2}} \log|\Delta X|$ for $\alpha = O(1)$. This result is quantitatively accurate only for step sizes much smaller than those used in the present calculations. Nevertheless, this nonlinear behaviour of the corner-stress error is supported by the numerical results, as discussed below. Rearranging the terms in (3.11), the tridiagonal matrix equation for the wall values of τ is obtained as

$$a_+\tau_{k-1,1} + \tau_{k,1} + a_-\tau_{k+1,1} = b_k, \tag{3.12a}$$

$$a_\pm = -\frac{1}{2}\left[\frac{(\Delta Z)^2 \pm \sigma\Delta X}{(\Delta X)^2 + (\Delta Z)^2}\right], \tag{3.12b}$$

$$b_k = \left[\frac{(\Delta Z)^2}{(\Delta X)^2 + (\Delta Z)^2}\right] \sum_{j=2}^{m-1} (\tau_{k+1,j} - 2\tau_{k,j} + \tau_{k-1,j}) + \left[\frac{(\Delta X)^2}{(\Delta X)^2 + (\Delta Z)^2}\right] \tau_{k,2}$$
$$+ \left\{\frac{\sigma\Delta X}{2[(\Delta X)^2 + (\Delta Z)^2]}\right\} (\tau_{k+1,2} - \tau_{k-1,2}) - \left[\frac{\Delta X \Delta Z}{(\Delta X)^2 + (\Delta Z)^2}\right] \alpha\delta_k^{kc}. \tag{3.12c}$$

The implicit nature of (3.12) allows instantaneous interaction of all shear profiles, which appears to aid in quickly suppressing downstream-growing eigenfunctions which might otherwise appear.

4. Results

Compression corners

Using the above numerical method, steady-state solutions of (2.2) and (2.3) have been obtained for a number of values of α, both positive and negative. Wall shear-stress distributions for compression ramps with corner angles ranging up to $\alpha = 3{\cdot}5$ are shown in figure 2. The non-dimensional shear stress τ is the ratio of the actual skin friction to the Blasius value for the undisturbed flow upstream.

Upstream of the corner the exponential approach to the uniform flow is quite rapid, while downstream the algebraic decay is noticeably slower. Near the corner, separated regions with reversed flow are indicated where $\tau_w < 0$. Careful calculations predict incipient separation for $\alpha = 1{\cdot}57$. For the unseparated cases ($\alpha = 1{\cdot}0$, $1{\cdot}5$), the abrupt change in the slope of τ_w *vs.* X at the corner is consistent with the linearized solution of Stewartson (1970*a*). Actually the linear theory predicts that

$$d\tau_w/dX \sim \alpha X^{-\frac{1}{3}} \quad \text{for} \quad X \to 0^+;$$

obviously a finite-difference computation on a uniform grid cannot resolve this singularity precisely.

For the nonlinear problem Jenson (1977) has treated the corner singularity following Goldstein's (1930) analysis for the conventional boundary layer. Jenson's analysis shows that on the downstream side of the corner

$$d\tau_w/dX \sim \pm 0{\cdot}7866|\tau_w|^{\frac{4}{3}}_{X=0}\alpha|X|^{-\frac{1}{3}} + O(\log|X|)$$

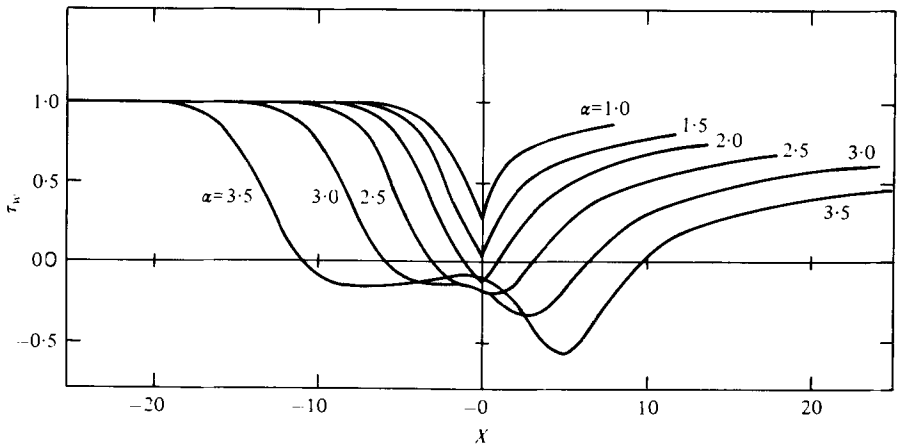

FIGURE 2. Compression-ramp wall shear distributions. $\sigma = 0$.

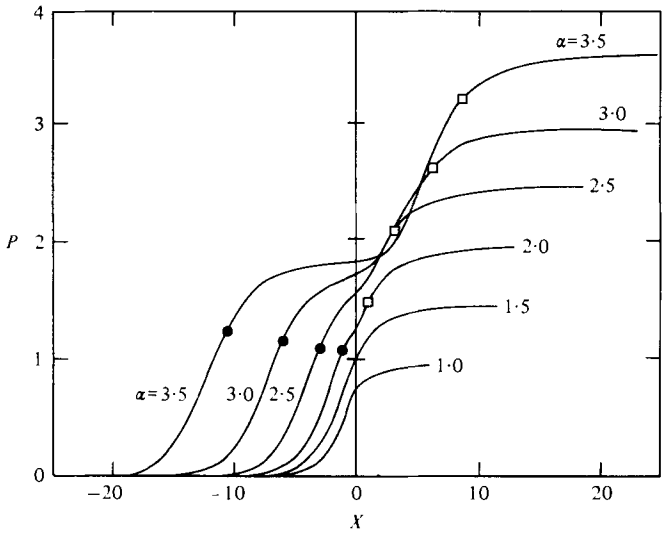

FIGURE 3. Compression-ramp pressure distributions. $\sigma = 0$.
●, separation point; □, reattachment point.

in the local flow direction from the corner (where the upper sign applies to unseparated cases, the lower sign to separated cases). For $\alpha = 2{\cdot}0$ the sign of the jump in $d\tau_w/dX$ given by this analysis contradicts that indicated by the numerical results. This discrepancy may be attributed to the fact that for the conditions of this case (small τ_w but large dP/dX at the corner) the Goldstein region is extremely short, much shorter than the mesh size. For larger values of α the Goldstein region is longer, but still has not been resolved completely by the finite-difference calculations. However, the trends indicated by the analysis can be seen in the numerical solutions. The step-size studies reported below indicate that the accuracy of the solutions outside the Goldstein region is not dependent on resolving the singularity. However, this singularity in $\tau_w \equiv \partial U/\partial Y$ is expected to be resolved on a length scale small compared with that of the triple deck.

	Mesh size		Mesh boundaries		
α	ΔX	ΔZ	$X_{\min}$	$X_{\max}$	$Z_{\max}$
1·0	0·3	0·3	−9·6	8·1	14·7
1·5	0·3	0·3	−8·7	12·0	14·7
2·0	0·3	0·3	−10·2	13·5	17·7
2·5	0·6	0·6	−17·4	18·0	29·4
3·0	0·6	0·6	−23·4	24·0	41·4
3·5	0·8	0·8	−27·2	52·0	63·2

TABLE 1. Computational mesh parameters for compression-ramp solutions shown in figures 2 and 3.

Pressure distributions for the compression ramps are shown in figure 3. When separation occurs, an inflexion point is seen to occur in the pressure distribution at the corner ($x = 0$). As α increases above the value for incipient separation, the inflexion develops into a constant-pressure plateau, which is quite evident for $\alpha = 3{\cdot}5$. The initial rise to the plateau level is pushed upstream with invariant shape as α increases, suggesting that as $\alpha \to \infty$ the separation point is pushed upstream to infinity; i.e. as α^* increases beyond the $Re^{-\frac{1}{4}}$ scale, the interaction length exceeds the $Re^{-\frac{3}{8}}$ scale. Conversely, one may say that for large α the corner lies infinitely far downstream of the separation point on the $Re^{-\frac{3}{8}}$ scale. For this case, Williams (1975) has shown that the plateau pressure asymptotes to the value 1·8, which is seen to be in good agreement with the results for $\alpha = 3{\cdot}5$.

Numerical mesh data for these cases are given in table 1. Convergence to the steady state was better for the smaller ramp angles. For $\alpha \leqslant 2{\cdot}5$, the terminal values of $\partial\tau/\partial t$ were less than $3{\cdot}3 \times 10^{-4}$ everywhere in the mesh. For larger values of α, the convergence rate was much slower and the runs were terminated with the maximum value of $\partial\tau/\partial t$ less than $7{\cdot}4 \times 10^{-4}$. Consequently, we view these large-α results as qualitatively correct, but not quantitatively as precise as the lower-α cases.

The effect of mesh size on compression-ramp solutions is indicated in figure 4, which shows the $\alpha = 2{\cdot}5$ wall shear-stress distributions for several values of ΔX. The mesh employed for these results covered the region $-17{\cdot}4 \leqslant X \leqslant 18, 0 \leqslant Z \leqslant 29{\cdot}4$. A course mesh is seen to produce an overly large interaction region. Upstream of the corner, the greatest truncation error occurs in the region of maximum pressure gradient. Near the corner the error approaches zero, but grows rapidly in the downstream region of large pressure gradient with algebraically slow decay in the terminal region of constant pressure.

Because of the strong effect of mesh size, it is desirable to extrapolate the solution to zero mesh width, thereby converting the first-order accurate upwind-difference scheme to second-order accuracy. However, if the extrapolated solution is to be considered reliable, it must be shown that the computed results exhibit a linear dependence upon ΔX. Figure 5 shows plots of the wall shear stress *vs.* ΔX at several X stations for the case $\alpha = 2{\cdot}5$. As indicated, the extrapolation is quite linear for the three smallest values of ΔX except at the corner itself, where the truncation error is nonlinear as discussed in relation to (3.11). Thus linear extrapolation is felt to be valid at all points except the corner, where the extrapolated shear must be regarded with reservation.

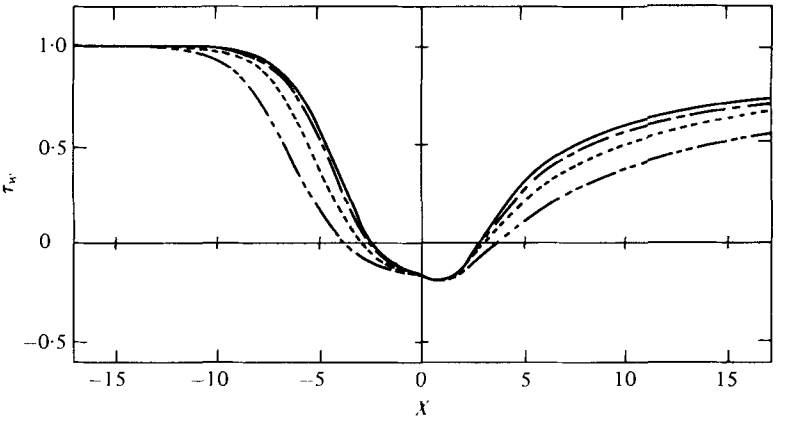

FIGURE 4. Effect of step size ΔX on compression-ramp wall shear distribution. $\sigma = 0$, $\alpha = 2{\cdot}5$, $\Delta Z = 0{\cdot}6$. ——, $\Delta X = 0{\cdot}2$; — — —, $\Delta X = 0{\cdot}3$; – – – – –, $\Delta X = 0{\cdot}6$; ——— —, $\Delta X = 1{\cdot}2$.

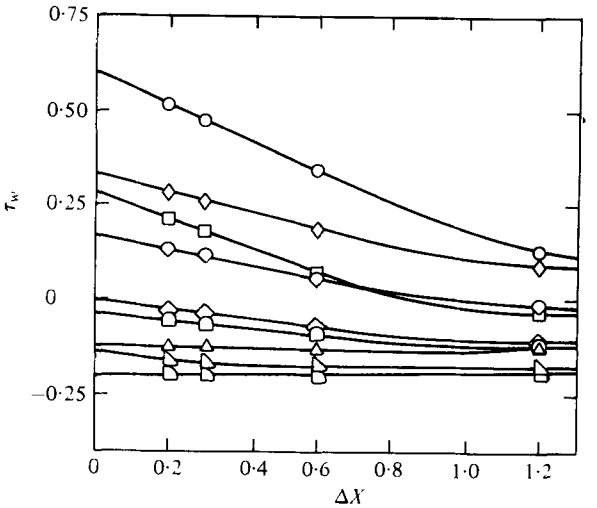

FIGURE 5. ΔX-extrapolation of compression-ramp wall shear. $\sigma = 0$, $\alpha = 2{\cdot}5$, $\Delta Z = 0{\cdot}6$. ○, $X = -4{\cdot}8$; □, $X = -3{\cdot}6$; ◇, $X = -2{\cdot}4$; △, $X = -1{\cdot}2$; ◺, $X = 0$; ◻, $X = 1{\cdot}2$; ⌓, $X = 2{\cdot}4$; ⬯, $X = 3{\cdot}6$; ◊, $X - 4{\cdot}8$.

The extrapolated wall shear distribution for $\alpha = 2{\cdot}5$ is compared with the accurate free-interaction solution of Stewartson & Williams (1969) in figure 6. The origin of both solutions is taken at the separation point. (Note that the origin is arbitrary in the Stewartson–Williams solution.) The agreement is excellent up to and slightly downstream of the separation point, where the $(\Delta X)^2$-accurate centred-difference scheme of Stewartson & Williams becomes unstable. As was noted earlier, the upstream pressure distribution and corresponding wall shear are pushed upstream with invariant shape as α increases above the incipient value. Hence, for the flow upstream of separation, this type of agreement with the Stewartson–Williams unique solution occurs for all separated ramp solutions ($\alpha > 1{\cdot}57$).

Corner shear profiles for several values of α appear in figure 7. For $\alpha = 3{\cdot}5$, the constant shear near the wall coincides with the development of the pressure plateau,

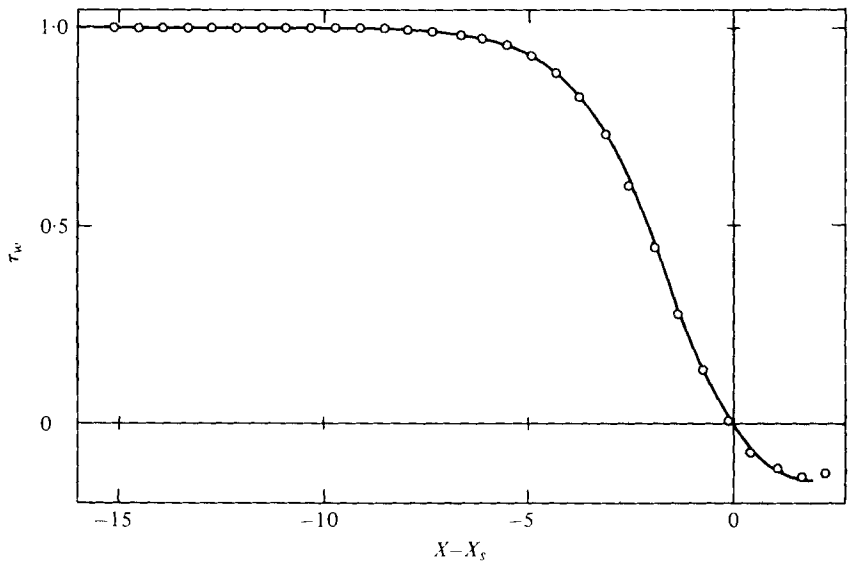

FIGURE 6. Comparison of compression-ramp wall shear distribution with free-interaction solution. ○, compression-ramp ΔX-extrapolated results, $\alpha = 2{\cdot}5$, $\Delta Z = 0{\cdot}6$, $\Delta X = 0{\cdot}2$, $0{\cdot}3$; ——, Stewartson–Williams solution.

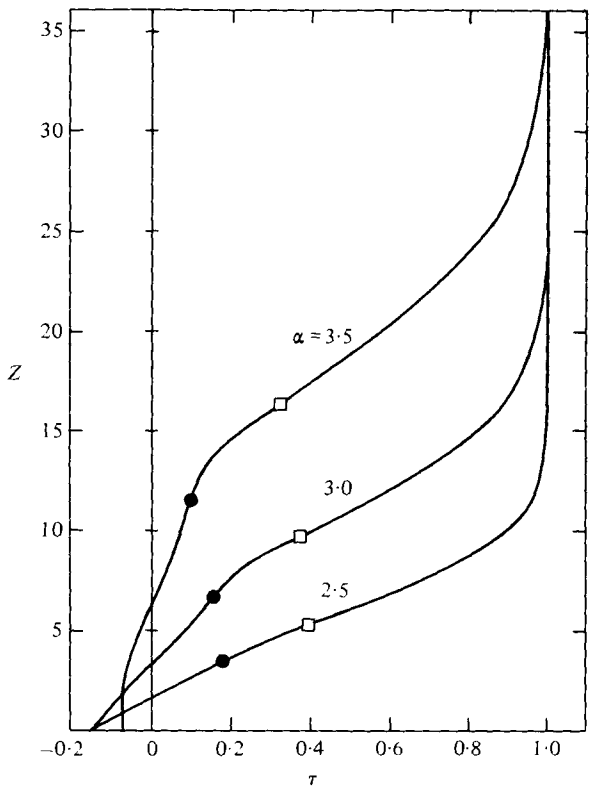

FIGURE 7. Compression-ramp corner shear profiles for $\sigma = 0$. ●, $u = 0$; □, $\psi = 0$. Mesh size as in table 1.

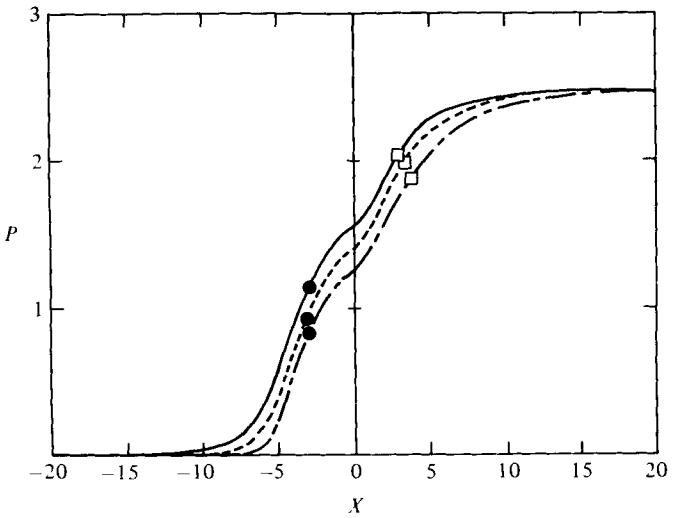

FIGURE 8. Effect of hypersonic parameter σ on compression-ramp pressure distribution. $\alpha = 2{\cdot}5$, $\Delta X = \Delta Z = 0{\cdot}6$. ——, $\sigma = 0$; – – –, $\sigma = 1$; ——, $\sigma = 2$; ●, separation point; □, re-attachment point.

consistent with the wall compatibility relation. A change in slope (near $\tau = 0{\cdot}2$) occurs for large α. Behaviour of this type is suggestive of the formation of a more complicated flow structure such as the development of a large inviscid core downstream of separation as described by Neiland (1970).

All of the foregoing results have been for the supersonic case, $\sigma = 0$. The effect of the hypersonic parameter σ upon the compression-ramp pressure distribution is indicated in figure 8. Solutions for $\alpha = 2{\cdot}5$ and several values of σ were generated using the same mesh sizes and mesh boundaries in each case. While the separation and reattachment points are only slightly affected, the pressure rise is seen to be delayed in X with increasing σ. For $\sigma = 2$, the pressure at the corner is about 80% of the $\sigma = 0$ value. The delayed pressure rise appears to be the predominant effect of σ upon the lower-deck solution. This produced a corresponding variation in the wall shear distribution; corner shear profiles for these cases, however, were practically identical.

At this point, it is appropriate to ascertain how well the asymptotic ($Re \to \infty$) lower-deck solutions approximate flows with finite Reynolds numbers. Werle & Vatsa (1973, 1974) have obtained solutions to the compressible boundary-layer equations for flow over compression ramps at finite Reynolds numbers, including the induced pressure rise due to the displacement effect. In order to confirm both their calculations and the present results a joint effort was carried out; the results are to be published separately (Burggraf *et al.* 1978) and are only summarized here. Only isolated comparisons between the triple-deck results and experimental data are possible, but Werle & Vatsa's results compare quite favourably with experiment and with the Navier–Stokes solutions of Carter (1971). Details of their method will be omitted here for brevity, although it may be mentioned that for the purposes of this comparison the pressure–displacement relationship was obtained from simple-wave theory.

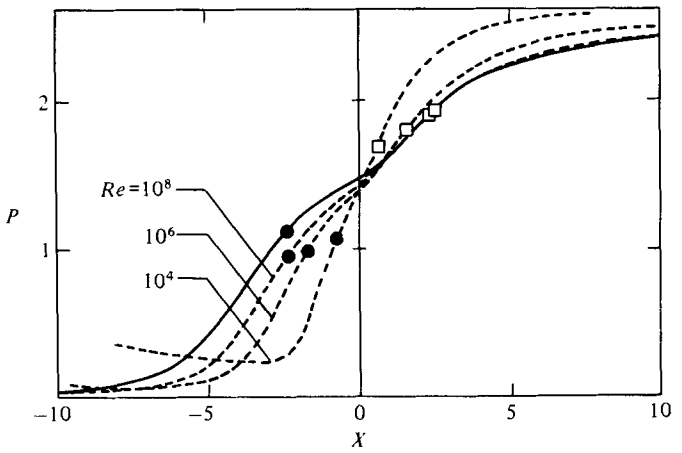

FIGURE 9. Comparison of compression-ramp pressure distribution with Werle–Vatsa solutions. $\alpha = 2{\cdot}5$, $M_\infty = 3{\cdot}0$, $T_\infty = 310°$ K, $T_w/T_{0\infty} = 0{\cdot}5$. ——, triple-deck solution; – – – –, Werle–Vatsa solutions; ●, separation point; □, reattachment point. All data ΔX-extrapolated.

For a systematic study of the effect of the Reynolds number, the case $\alpha = 2{\cdot}5$ was selected as representative of compression-ramp solutions which exhibit reversed-flow regions. As the interacting boundary-layer formulation does not permit solutions characterized by a single parameter (α), flow conditions were established for the problem. These were chosen as $M_\infty = 3{\cdot}0$, $Pr = 0{\cdot}71$, $T_\infty = 310$ °K and $T_w/T_{0\infty} = 0{\cdot}5$. With these conditions, a family of solutions for varying Reynolds number was generated with α held constant, corresponding to variation of the physical ramp angle α^*. All results were extrapolated to zero mesh width, as was the corresponding triple-deck solution.

Figure 9 shows the comparison of the triple-deck pressure distribution with the Werle–Vatsa solutions for several Reynolds numbers, plotted in lower-deck variables.† The falling upstream pressure, especially evident for $Re = 10^4$, is attributed to the weak-interaction solution of Lees & Probstein, which was used to initiate the Werle–Vatsa calculations. This characteristic is seen to diminish as the Reynolds number increases. These upstream displacement effects are neglected in the triple-deck formulation. The pressure everywhere upstream of the corner and the location of the separation point appear to approach the triple-deck values in the limit as $Re \to \infty$. However, at finite Reynolds numbers, the pressure level at separation is not accurately predicted by the limiting theory. This tendency to overpredict the separation pressure appears to be a weakness of the first-order triple-deck theory with regard to engineering applications. The downstream triple-deck solution seems to be the limit (as $Re \to \infty$) of the finite Reynolds number calculations, even at the corner and the reattachment point.

At the high Reynolds numbers indicated in this comparison, any physical flow would be expected to be turbulent, whereas the results shown are based upon the assumption of laminar flow. While this assumption places a severe constraint upon

† Actually the Werle–Vatsa computer program requires that the corner angle be slightly rounded; hence for consistency the triple-deck results in figure 9 were computed for the same rounded-corner geometry.

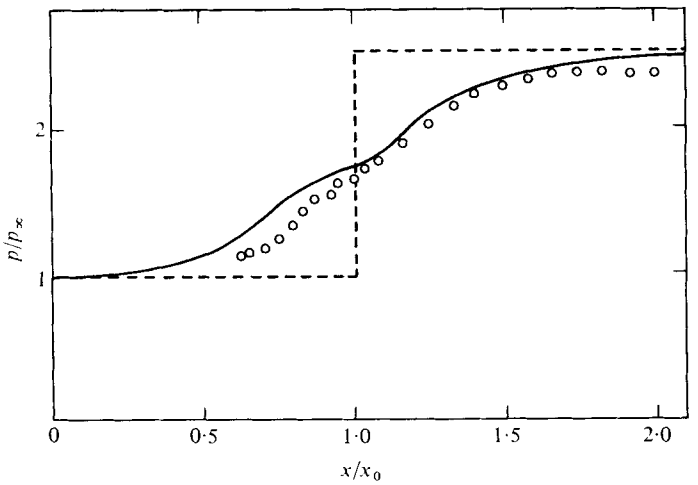

FIGURE 10. Comparison of compression-ramp pressure distribution with experiment. $\alpha = 2{\cdot}5$. – – – –, inviscid pressure rise; ——, ΔX-extrapolated numerical solution; ○, Lewis *et al.* experimental data, $\alpha^* = 10°$, $M_\infty = 4{\cdot}0$, $Re = 68\,000$, adiabatic wall.

physical applications for adiabatic wall conditions, transition can be delayed to very high Reynolds numbers with cooled walls. Thus triple-deck solutions may be used to provide an adequate description for flows of practical interest. In addition, comparison with finite Reynolds number solutions indicates that the triple-deck scalings are correct and should be accounted for in computing viscous–inviscid interacting flows.

A direct comparison of the triple-deck pressure distribution for $\alpha = 2{\cdot}5$ with the experimental data of Lewis, Kubota & Lees (1968) is made in figure 10. The test conditions correspond to adiabatic flow over a 10° ramp at $M_\infty = 4{\cdot}0$ with $Re = 6{\cdot}8 \times 10^4$ based on the distance to the corner. For this choice of flow parameters, it was found that the linearized simple-wave boundary condition underpredicts the ramp pressure rise by about 20%. To correct for this effect, the numerical results were used to obtain the flow angle from linear theory, and the pressure was then deduced from the exact Prandtl–Meyer pressure/flow-angle relationship. As was noted earlier, the triple-deck solution appears to overpredict the pressure rise upstream of the corner. Downstream, the triple-deck solution is asymptotic to the inviscid pressure rise while the experimental data fall somewhat below this level.

Expansion corners

While the unsteady numerical procedure outlined in §3 has been formulated specifically to obtain reversed-flow solutions, the method may be applied intact to expansion corners by merely requiring $\alpha < 0$. Stewartson (1970*b*) has previously considered expansion corners for the supersonic case only. For $|\alpha| \ll 1$ he obtained a linearized solution and for larger values of α employed an indirect method to solve the lower-deck equations. This technique established the upstream solution by prescribing a small pressure perturbation at some value of X ahead of the corner and marching downstream to $X = 0$. At the corner, a value of α was assumed and a downstream solution generated. The value of α was then iterated upon until the downstream pressure attained a constant level. Because of the marching technique

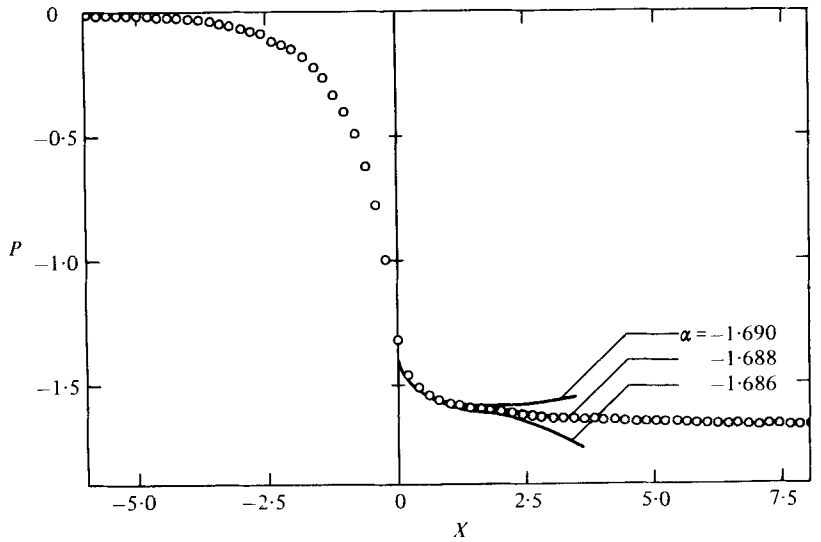

FIGURE 11. Expansion-ramp pressure distribution. ——, Stewartson solution; ○, present numerical results (ΔX-extrapolated), $\alpha = -1{\cdot}689$, $\Delta Z = 0{\cdot}3$, $\Delta X = 0{\cdot}1$, $0{\cdot}2$.

employed, Stewartson's numerical results were second-order accurate and subsequently extrapolated to zero mesh width, and thus are thought to be quite reliable.

Because of the favourable pressure gradient induced by an expansion, the flow is accelerated and produces a decrease in both the X and the Z extent of the interaction region as the expansion angle increases. Thus it is necessary to employ a reasonably fine numerical mesh if the details of the flow are to be properly resolved. As in the compression case, numerical mesh-size studies indicated that the results could be extrapolated to zero mesh width in order to improve accuracy. Figure 11 provides a comparison of extrapolated results with the accurate solution of Stewartson for the case $\alpha = -1{\cdot}689$. The upstream solution of Stewartson was not given in his results. Downstream, his pressure distributions indicate the behaviour for several choices of α with a fixed upstream solution. The slight disagreement of the two results, particularly at the corner, is attributed to the higher accuracy in Stewartson's calculation.

In figure 12, the pressure distributions for two values of α are given, with the non-dimensional pressure P normalized by α. This choice of variables allows a direct comparison with the linearized solution of Stewartson (1970*a*) for $|\alpha| \ll 1$. As α decreases ($|\alpha|$ increases), it is seen that the X extent of the interaction region collapses to the immediate vicinity of the corner. For small values of $-\alpha$, the solution is very much like the linear result. In fact, the case $\alpha = -1$ has been omitted from the figure as it was virtually indistinguishable from the linear solution. For each of the cases shown the pressure at the corner is $0{\cdot}75\alpha$. An analysis by Stewartson shows that the entire pressure drop occurs upstream of the corner for $\alpha \to -\infty$. Our numerical results for large negative α indicate a moderate trend in this direction, but truncation error was sufficiently large that these results must be considered tentative and are not presented here.

Corresponding wall shear distributions for these cases appear in figure 13. Here the perturbation of the wall shear from its undisturbed value has been normalized by α

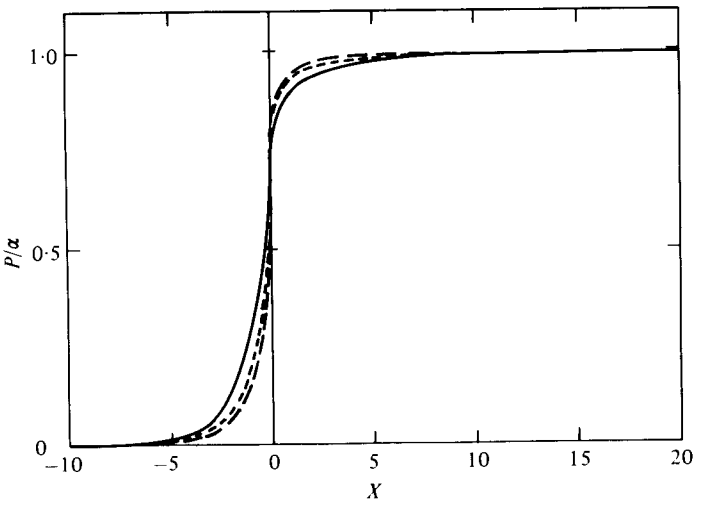

FIGURE 12. Expansion-ramp pressure distributions. $\sigma = 0$. ——, linearized solution; – – – –, $\alpha = -2$; — —, $\alpha = -3$. Numerical results ΔX-extrapolated; $\Delta Z = 0{\cdot}3$, $\Delta X = 0{\cdot}3$, $0{\cdot}6$.

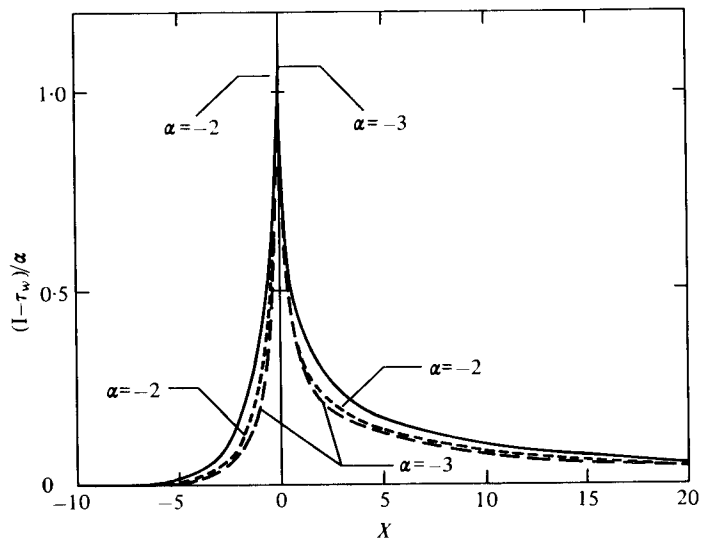

FIGURE 13. Expansion-ramp wall shear distributions. $\sigma = 0$. ——, linearized solution; – – – –, $\alpha = -2$; — —, $\alpha = -3$. Numerical results ΔX-extrapolated; $\Delta Z = 0{\cdot}3$, $\Delta X = 0{\cdot}3$, $0{\cdot}6$.

for comparison with the linear result. The distributions are again seen to vary slowly from the linear solution as $|\alpha|$ increases. As in the compression-ramp solutions, the slow downstream algebraic return to the undisturbed profile is evident.

Figure 14 provides corner shear profiles for several negative values of α. The marked increase in the corner wall shear for increasing $|\alpha|$ is quite apparent, as well as the thinness of the lower deck. It is seen that the outer-edge value of τ for $\alpha = -3$ is attained at $Z \simeq 3$; by comparison, for $\alpha = +3$ the outer-edge value is reached at $Z \simeq 24$ (see figure 7).

Turning to the hypersonic case, pressure distributions for $\alpha = -1$ for several

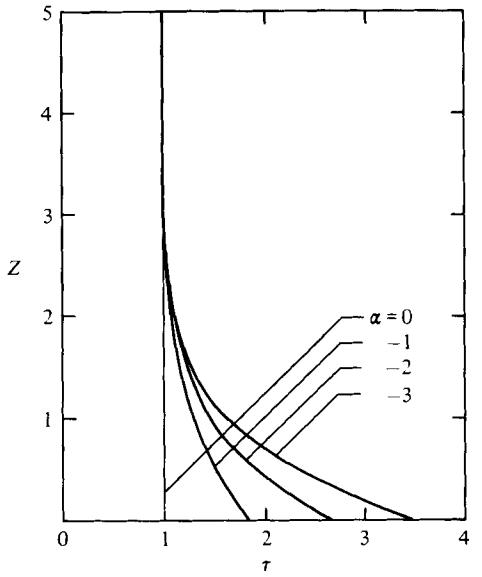

FIGURE 14. Expansion-ramp corner shear profiles. $\sigma = 0$, $\Delta X = \Delta Z = 0{\cdot}6$.

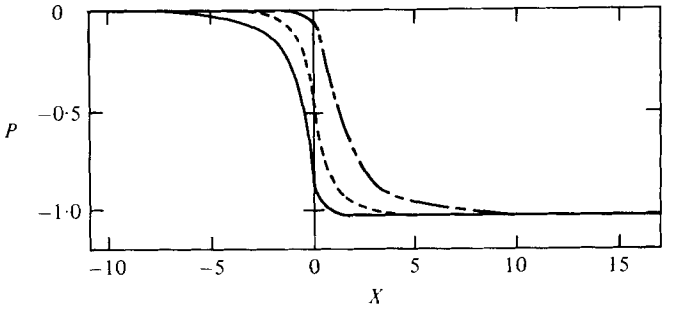

FIGURE 15. Effect of hypersonic parameter σ on expansion-ramp pressure distribution. $\alpha = -1$, $\Delta X = \Delta Z = 0{\cdot}6$. ——, $\sigma = 0$; – – – –, $\sigma = 1$; — — —, $\sigma = 2$.

values of σ are given in figure 15. As with the compression-ramp results, an increase in σ noticeably shortens the interaction zone upstream while extending it downstream. This results in a drastic change in the corner pressure, which for $\sigma = 2$ is seen to be only slightly different from the undisturbed value.

5. Conclusions

An unsteady numerical technique has been formulated to solve the steady supersonic and hypersonic triple-deck equations for flows past compression and expansion corners. Numerical results were extrapolated to zero mesh width to obtain accurate solutions for both separating and non-separating flows. In the case of supersonic flow, the results consist of a one-parameter family of solutions depending only upon the reduced corner angle α. Comparisons with both finite Reynolds number solutions and experiment indicate that first-order triple-deck theory, while correct asymptotically,

is only qualitatively accurate unless applied at very high Reynolds numbers. Nevertheless, the scalings of the inner layer appear to be correct and should not be violated in numerical studies if the interaction region is to be properly described.

The authors are grateful to the Office of Naval Research, which sponsored the research described here under Contract No. N00014-67-A-0232-0014.

REFERENCES

BROWN, S. N., STEWARTSON, K. & WILLIAMS, P. G. 1975 *Phys. Fluids* **18**, 633.

BROWN, S. N. & WILLIAMS, P. G. 1975 *J. Inst. Math. Appl.* **16**, 175.

BURGGRAF, O. R. 1975 *AGARD Current Paper* no. 168.

BURGGRAF, O. R., RIZZETTA, D. P., WERLE, M. J. & VATSA, V. N. 1978 To be published.

CARTER, J. E. 1971 Ph.D. dissertation, Virginia Polytechnic Institute and State University.

CHAPMAN, D. R., KUEHN, D. M. & LARSEN, H. K. 1958 *N.A.C.A. Rep.* no. 1356.

CROCCO, L. & LEES, L. 1952 *J. Aero. Sci.* **19**, 33.

GOLDSTEIN, S. 1930 *Proc. Camb. Phil. Soc.* **26**, 1.

JENSON, R. 1977 Ph.D. dissertation, The Ohio State University.

JENSON, R., BURGGRAF, O. R. & RIZZETTA, D. P. 1975 *Proc. 4th Int. Conf. Numer. Meth. Fluid Mech., Lecture Notes in Phys.* **35**, 218.

LEES, L. & REEVES, B. L. 1964 *A.I.A.A. J.* **3**, 303.

LEWIS, J. E., KUBOTA, T. & LEES, L. 1968 *A.I.A.A. J.* **6**, 7.

LIGHTHILL, M. J. 1950 *Quart. J. Mech. Appl. Math.* **3**, 303.

LIGHTHILL, M. J. 1953 *Proc. Soc. Roy.* A **217**, 478.

MESSITER, A. F. 1970 *SIAM J. Appl. Math.* **18**, 241.

NEILAND, V. Y. 1969 *Mekh. Zh. i. Gaza* **4**, 40.

NEILAND, V. Y. 1970 *Izv. Akad. Nauk SSSR* **3**, 19.

RIZZETTA, D. P. 1976 Ph.D. dissertation, The Ohio State University.

ROSENHEAD, L. (ed.) 1963 *Laminar Boundary Layers*, Oxford: Clarendon Press.

SMITH, F. T. & STEWARTSON, K. 1973 *Proc. Roy. Soc.* A **332**, 1.

STEWARTSON, K. 1970*a* *Quart. J. Mech. Appl. Math.* **23**, 137.

STEWARTSON, K. 1970*b* *Proc. Roy. Soc.* A **319**, 289.

STEWARTSON, K. 1974 *Adv. Appl. Math.* **14**, 145.

STEWARTSON, K. & WILLIAMS, P. G. 1969 *Proc. Roy. Soc.* A **312**, 181.

WERLE, M. J. & VATSA, V. N. 1973 *Aerospace Res. Labs. (USAF) Rep.* ARL-73-0162.

WERLE, M. J. & VATSA, V. N. 1974 *A.I.A.A. J.* **12**, 1491.

WILLIAMS, P. G. 1975 *Proc. 4th Int. Conf. Numer. Meth. Fluid Mech., Lectures Notes in Phys.* **35**, 445.